

B. Hnat, S. Gadgil, A. Kirk, F. Militello, N. Walkden and
the MAST Team

Experimental constraint on the radial mode number of the Geodesic Acoustic Mode in MAST Ohmic plasma

Enquiries about copyright and reproduction should in the first instance be addressed to the Culham Publications Officer, Culham Centre for Fusion Energy (CCFE), K1/083, Culham Science Centre, Abingdon, Oxfordshire, OX14 3DB, UK. The United Kingdom Atomic Energy Authority is the copyright holder.

Experimental constraint on the radial mode number of the Geodesic Acoustic Mode in MAST Ohmic plasma

B. Hnat¹, S. Gadgil¹, A. Kirk², F. Militello², N. Walkden² and the MAST Team

¹ *Physics Department, University of Warwick, Coventry, CV4 7AL, UK.*

² *EURATOM/CCFE Fusion Association, Culham Science Centre, Abingdon, OX14 3DB, UK.*

Experimental constraint on the radial mode number of the Geodesic Acoustic Mode in MAST Ohmic plasma.

B. Hnat¹, S. Gadgil¹, A. Kirk², F. Militello², N. Walkden² and the MAST Team

¹ Physics Department, University of Warwick, Coventry, CV4 7AL, UK.

² EURATOM/CCFE Fusion Association, Culham Science Centre, Abingdon, OX14 3DB, UK.

E-mail: b.hnat@warwick.ac.uk

Abstract. Reciprocating Mach probe data is used to estimate the radial wave number of oscillatory zonal flows in Ohmic MAST plasma. An intermittent ~ 10 kHz mode is detected in the wavelet decomposition and windowed spectra of plasma potential fluctuations of the MAST tokamak edge plasma. Previously, this mode has been identified as a Geodesic Acoustic Mode (GAM) using probe observations and numerical simulations. Two-points phase differencing technique applied to probe pins with radial and poloidal separations give an estimate of the radial wave number at the desired range of frequencies. The phase velocity of propagation and an estimate of the shearing rate of the GAM is then obtained. We measure the radial mode number to be $0.05 \leq k_r \rho_p \leq 0.15$ and a radial propagation speed of up to ~ 1 km/s. The GAM shearing rate is an order of magnitude smaller than the growth rate of drift-like turbulence. These results are consistent with the estimates obtained previously from multi-fluid numerical simulations of GAM in MAST.

PACS numbers: 52.55.Fa, 52.35. Ra, 52.30.-q, 52.35.Mw, 52.35.Py

Submitted to: *Plasma Phys. Control. Fusion*

1. Introduction

The anisotropic properties of drift turbulence (DT) lead to the development of large scale sheared flows, known as zonal flow (ZF) [1]. These flows can regulate the global confinement properties of the magnetically confined plasma by suppressing turbulent transport across the magnetic field [2, 3]. It is believed that zonal flows are essential in the transition to high-confinement mode (H-mode), with the edge plasma turbulence being substantially reduced during the transition [4, 5, 6]. In slab geometry, zonal flows are stationary and have zero frequency, that is their radial group velocity is zero [7]. In toroidal geometry, the curvature and the inhomogeneous magnetic field induce two effects: radial propagation of these modes and the coupling of electrostatic potential structures with poloidal mode number $m = 0$ to density fluctuations with higher m numbers and with finite frequency. This finite frequency compressible oscillation is called geodesic acoustic mode (GAM). The local dispersion relation for the GAM has been derived from various plasma models and the leading term is $\omega_{GAM,l} \sim c_s/R_0$, where c_s is the local sound speed and R_0 is the major radius [8, 9, 10, 11]. Compressible GAM fluctuations are heavily Landau damped for small safety factors $q(r) \equiv rB_t/R_0B_p$, where B_t and B_p are toroidal and poloidal magnetic field components, respectively. In the usual tokamak configuration and in the low-confinement mode (L-mode) $q(r)$ increases toward the edge of the plasma and thus GAMs are confined to the edge region in L-mode plasmas. There is substantial evidence that the GAM is a global mode, with a complex radial mode structure that does not simply follow the linear local dispersion relation. Indeed, observations [12, 13, 14, 15] and numerical simulations [16, 17] found a series of plateaus with nearly constant frequency spanning large fractions of minor radius. The aim of this work is to estimate the characteristic size of this radial structure based on Langmuir Mach probe measurements at the edge region of the Ohmic MAST plasmas.

The radial propagation of oscillatory zonal flows and the presence of compressible GAM fluctuations add new physics to the ZF-GAM-DT interactions. GAM pressure fluctuations are nonlinearly advected by ZF and can transfer the energy to small scales providing a natural saturation mechanism for the zonal flow amplitudes [18]. In terms of linear effects, GAMs introduce new spatial and temporal scales into the system. The GAM radial mode number k_r gives a shearing rate of turbulent eddies $\gamma_{sh} \approx k_r V_{E \times B}$, where $V_{E \times B}$ is the poloidal zonal flow amplitude. The importance of the shearing mechanism depends on a time scale τ_{k_r, p_r} , which reflects temporal coherence of turbulence wave packets, with mode number p_r , and the GAM [19]. We note the appearance of the GAM group velocity, due to its finite frequency, also permits some resonant-like interactions between GAMs and the turbulence. For example, taking $\tau_{k_r, p_r} \sim |(v_{gr}^{GAM} - v_{ph}^{GAM})k_r|^{-1}$ we obtain an infinite correlation time of turbulent structure propagating with the group velocity $v_{gr}^{DT} = v_{ph}^{GAM}$.

The simplest analytical estimate of the GAM group velocity assumes that the diamagnetic current, due to an inhomogeneous magnetic field and its curvature, is closed by the ion polarisation current [20]. Then, the finite gyroradius effects lead to

the expression $(1 - k_r^2 \rho_p^2) \omega_{GAM}^2 = \omega_{GAM,l}^2$, where ρ_p is the proton gyroradius. Qualitative arguments, based on results of numerical simulations, can be used to constrain k_r . Numerical studies have found the most unstable mode for drift/ITG turbulence at $k_\theta \rho_p \approx 0.3$. Nonlinear interactions of turbulent structures transfer the energy to larger spatial scales, thus it is assumed that GAM's radial wave number obeys $k_r \rho_p < 0.3$. Global multi-fluid simulations have also been used to model GAMs directly, for the realistic MAST like Ohmic discharges. These simulations found a relatively narrow range of wave numbers $k_r \rho_p \approx 0.05 - 0.15$ [15].

Here, we use MAST reciprocating Mach probe data to estimate the value of k_r directly, using the instantaneous phase difference technique applied to radially and poloidally separated probe pins measuring the electrostatic plasma potential. We employ a modified Beall algorithm [21], in which the use of windowed Fourier decomposition has been replaced by a wavelet transform. This allows us to obtain statistically significant estimates of the wave number for short time intervals when the reciprocating probe position is relatively constant. Our results are consistent with previous numerical studies and give estimates of $0.05 < k_r \rho_p < 0.15$. We find more power at larger wave numbers when the probe is approximately 2.5 cm from the LCFS and a small wave number of $k_r \rho_p \sim 0.05$ when the probe is near its maximum displacement of 4.5 cm inside the plasma.

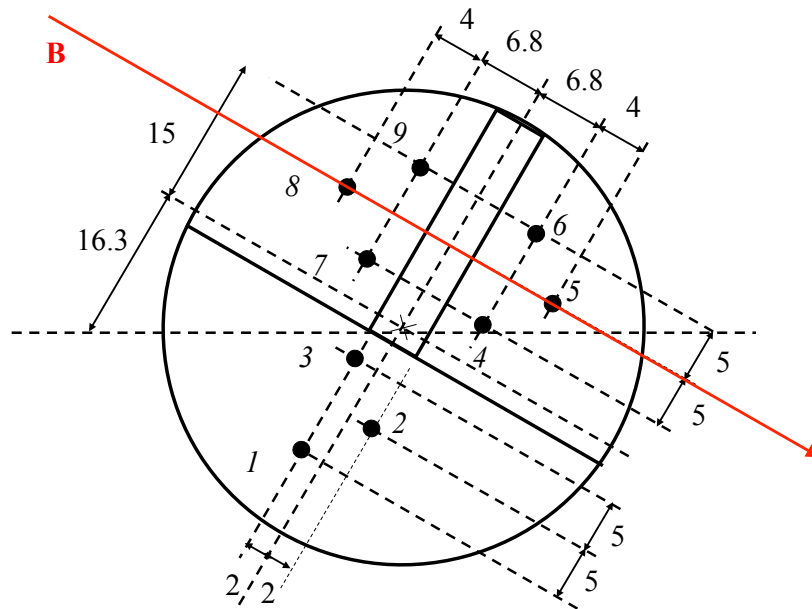


Figure 1. (a) Langmuir Mach probe with separations of different pins. Pins 1,2 and 3 are radially offset by 8mm from all other pins.

2. Data

MAST is a spherical tokamak with a major radius $R_0 \approx 0.95$ m and a minor radius of $a \approx 0.65$ m, magnetic field strength is about 0.5T with the toroidal, B_t , and the poloidal, B_p , field components giving a pitch angle of about 22° at the edge region. We analyse data from an Ohmic plasma discharge numbered 29150, with a line average number density, $n \approx 1.47 \times 10^{19} \text{ m}^{-3}$, and plasma current $I_p = 0.43\text{MA}$. No additional heating power was applied during the discharge. The data was collected using a Mach type reciprocating Langmuir probe [22], on the outboard mid-plane, measuring floating potential, \tilde{V}_f as well a set of ion saturation currents. Figure 1 shows the schematic of the probe, with pin numbers and the relative distances between them. Pins (1, 3) are positioned 8 mm behind pin pairs (4, 6) and (7, 9).

Figure 2 presents a summary of the data. Panel (a) shows wavelet power in the floating potential of pin 3 as a function of time. We observe a clear but intermittent increase of power in a relatively narrow frequency range of ~ 9 to ~ 15 kHz between times 0.30 and 0.39 seconds of the discharge. We have verified that there is no significant magnetic activity at this time. Panel (b) of Figure 2 shows the distance of the Mach probe in relation to the last closed flux surface (LCFS). The probe is inside the plasma and reaches the maximum radial location of about 5 cm at the time of 0.35 seconds. Panel (c) of Figure 2 shows electron temperature from Thompson scattering diagnostic at the time of interest. It gives the electron temperature at the probe location of $T_e \approx 10\text{eV}$. The proton gyroradius at the electron temperature is $\rho_p = 0.15$ cm.

We analyse floating potential data, $\tilde{V}(\mathbf{x}_i, t)$, where $i = 1, 3, 7, 9$ indicates the relevant pin number and vector \mathbf{x} is a position of each pin. We choose three intervals spanning periods 0.30 – 0.325, 0.34 – 0.36 and 0.36 – 0.38 seconds when the probe distance to the LCSF is relatively stable. We will refer to these intervals as A , B and C . The average probe position in each interval is $D_A = -2.53$ cm, $D_B = -4.00$ cm and $D_C = -3.14$ cm. Each interval contains at least 1×10^4 samples. Numerical simulations of L-mode discharge with realistic shaping parameters found strong GAM oscillations in a broad range of radii ($0.9 < \psi^{1/2} < 1$), with the maximum of power located at $0.95 < \psi^{1/2} < 0.975$, for the 10 kHz harmonic [17]. In addition, previous analysis of MAST reciprocating probe data identified a strong 10 kHz signal with a GAM-like dispersion relation [15]. Based on these findings, we interpret observed 9 – 15 kHz oscillations as due to the GAM.

Figures 3 and 4 show details of spectral and temporal features of the data for intervals A and B , respectively. Both figures show: wavelet power in panels (a), time integrated wavelet power spectrum, for the same frequencies as shown on the y-axis in panels (a), and a short time series of the floating potential $\tilde{V}(\mathbf{x}_3, t)$ and $\tilde{V}(\mathbf{x}_7, t)$ filtered between 5 and 15 kHz, in panels (c). We note a significant difference in the power spectra of the intervals A and B . Interval A has a narrow spectral peak at ~ 10 kHz, while the spectral peak of interval B is much broader, with significant power in the range of ~ 9 to ~ 15 kHz. Various numerical simulations demonstrated the

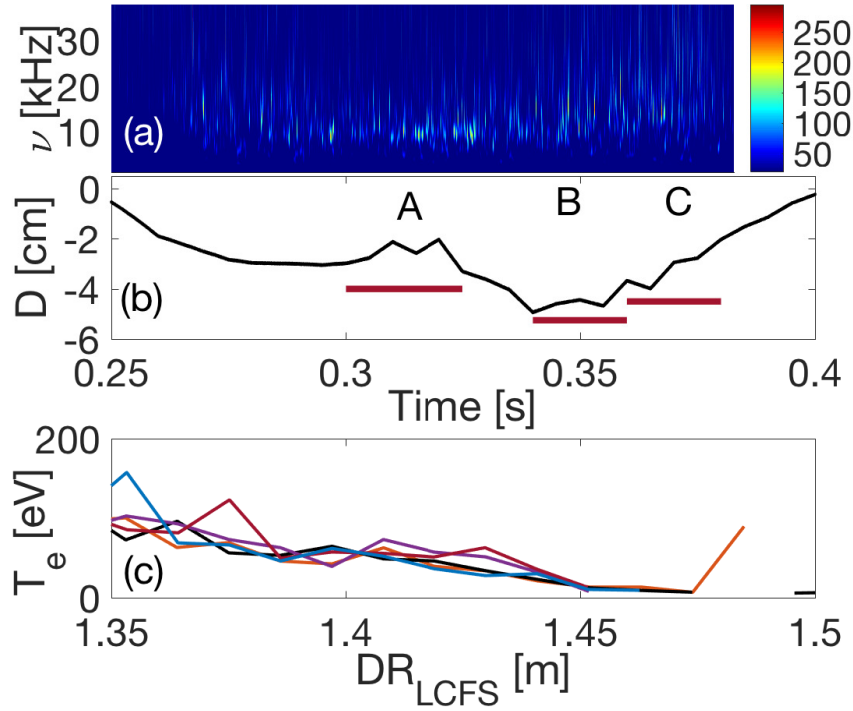


Figure 2. Summary of the data. (a) Wavelet power at lower frequencies. (b) Mach probe distance from the last closed flux surface (LCFS); negative values indicate position inside the plasma. Horizontal red lines mark three time intervals analysed here. (c) Electron temperature profiles from Thompson scattering system between 0.32 – 0.36 seconds.

emergence of frequency plateaus spanning some fraction of a minor radius, with higher harmonic plateaus sometimes overlapping with the main harmonic one [17]. The power distribution of interval *B* is consistent with a double plateau at ~ 10 and ~ 15 kHz. Panels (c) of Figures 3 and 4 demonstrate that the signals on both pins are similar, and that the phase shift between these varies, but is always smaller than the wavelength of the large amplitude fluctuations.

3. The Methodology

We apply the data analysis technique which uses a two-point instantaneous phase difference to extract the wave number from the signal. Ordinarily, this technique is used when the connection vector $\mathbf{d} = \mathbf{r}_1 - \mathbf{r}_2$ between the measurements points \mathbf{r}_1 and \mathbf{r}_2 is approximately aligned with the wave vector. In such case, an estimate of the wave vector projection on the connection vector $k_p = \mathbf{k}(\nu) \cdot \mathbf{d}$ is obtained in four steps. First, the wavelet transform is calculated giving a coefficient $W(\mathbf{r}_i, \nu, \tau)$ for each frequency ν (scale) at each measurement time τ . Second, the instantaneous cross-spectral density, $H(\mathbf{d}, \nu, \tau)$ is obtained as follows:

$$H(\mathbf{d}, \nu, \tau) = W^*(\mathbf{r}_1, \nu, \tau)W(\mathbf{r}_2, \nu, \tau) = |W| \exp(i\phi). \quad (1)$$

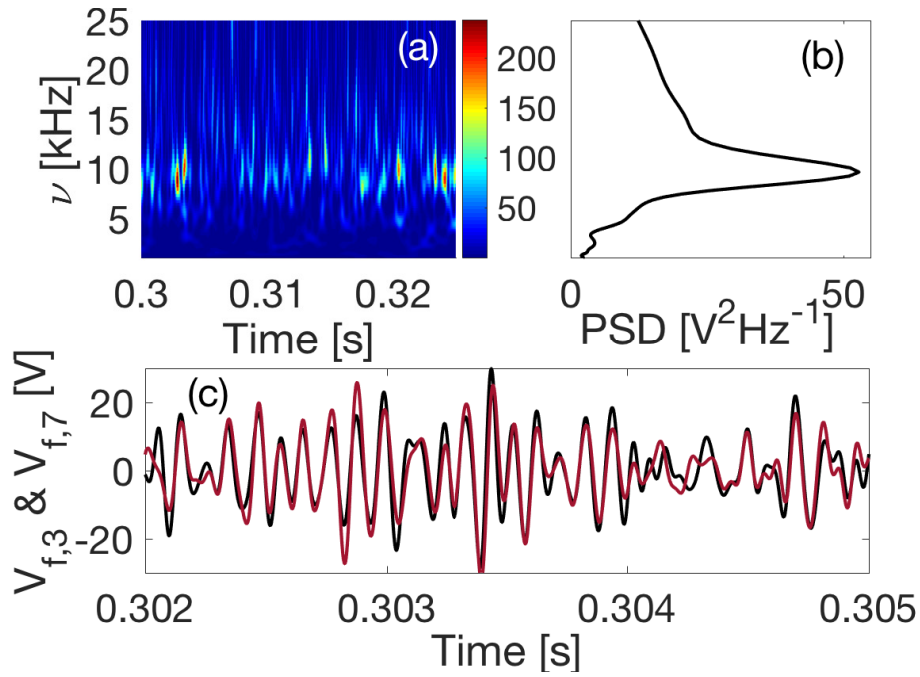


Figure 3. Summary of the data for interval A. (a) Wavelet power at lower frequencies, units [V² Hz⁻¹]. (b) Integrated wavelet power. (c) Time series of the floating potential from pins 3 (black line) and 7 (red line) for small time interval.

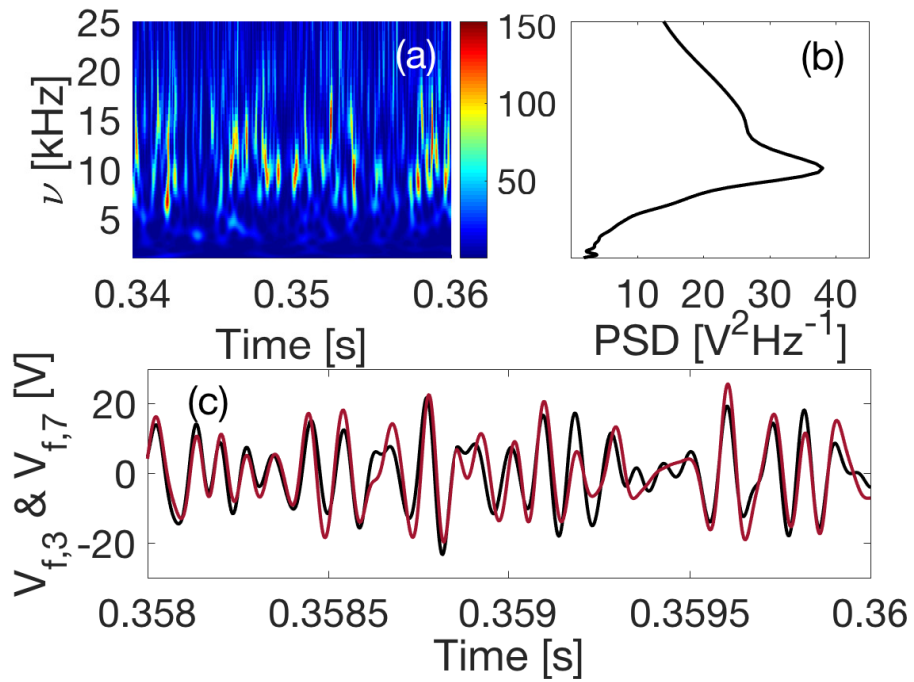


Figure 4. Same as figure 3, but for interval B.

The last equality expresses the complex quantity $H(\mathbf{d}, \nu, \tau)$ in polar representation and defines the instantaneous phase as $\phi(\mathbf{d}, \nu, \tau) = \arctan[\Im(H(\mathbf{d}, \nu, \tau))/\Re(H(\mathbf{d}, \nu, \tau))]$. The third step gives an estimate of the projected wave number

$$k_p(\nu) \approx \frac{\phi(\nu)}{d}. \quad (2)$$

Finally, having established a relation between the wave number and the frequency, a histogram of power at each (k_p, ν) pair is constructed according to

$$S(k_p, \nu) = \left\langle \frac{1}{2} (|W(\mathbf{x}_i, \nu, \tau)|^2 + |W(\mathbf{x}_i, \nu, \tau)|^2) \delta(k - k_p) \right\rangle. \quad (3)$$

where angular brackets now indicate an ensemble average over all measurement points. In practice, $S(k_p, \nu)$ is calculated by binning instantaneous power given by (6) into a discretised (k_p, ν) plane. The wavenumber-frequency spectrum $S(k_p, \nu)$, when examined visually, can reveal multiple dispersion relations in the system. The definition of the projected wave number (2) introduces a natural ambiguity of $2j\pi$ ($j \in \mathbb{Z}$) and, in principle, the domain of k_p spans an infinite number of negative and positive values of j . The visual inspection of the $S(k_p, \nu)$ plot can easily reveal if such an ambiguity is present.

The basic method described above cannot yield the radial wave number in the case of Mach probe data, without further assumptions. Indeed, the radial separation of pins 3 and 7 is comparable to their poloidal separation and the wave vector direction is not, in principle, aligned with the overall separation vector. While GAM poloidal wave number should be small, compared to its radial component, field-aligned density filaments generated by turbulence contribute to poloidal correlations on the intermediate spatial scales. We now describe the details of the modified method, which uses pin pairs (1, 3) and (7, 9) to compensate for the poloidal wave number contribution to the radial wave number obtained from pair (3, 7).

As with the basic method, the instantaneous phase difference $\phi(t)$ between spectral components of a signal is estimated from cross-coherence, constructed from the wavelet decomposition. The analysed data is a floating potential offset by its time average, $V(\mathbf{x}_i, t) = \tilde{V}(\mathbf{x}_i, t) - \langle \tilde{V}(\mathbf{x}_i, t) \rangle_t$. We assume that $V(\mathbf{x}_i, t)$ represents a zero-mean, stationary, homogeneous scalar field, which can be represented as a superposition of plane wave packets using wavelet decomposition with the wavelet coefficients given by

$$W(\mathbf{x}_i, s, \tau) = \int_{-\infty}^{\infty} dt V(\mathbf{x}_i, t) \frac{1}{\sqrt{s}} \psi^* \left(\frac{t - \tau}{s} \right), \quad (4)$$

where s is a scale, τ is a new time and $\psi(t)$ are the analysing wavelets. We use Morlet wavelets defined as

$$\psi(t) = \frac{1}{\pi^{1/4}} \exp(-2\pi it) \exp(-t^2/2), \quad (5)$$

which have good simultaneous time-frequency resolution and are mathematically identical to a Fourier transform with a short-time Gaussian window function. The scale s can be related to an instantaneous angular frequency $\omega = 2\pi/s$. Since all results

will use frequency ν (in kHz), rather than the angular frequency ω , we will deviate from the standard notation and use frequency in the equations that follow. The time averaged power spectrum of a single point data collected at pin location \mathbf{x}_i is then expressed as

$$P(\mathbf{x}_i, \nu) = \langle W^*(\mathbf{x}_i, \nu, \tau)W(\mathbf{x}_i, \nu, \tau) \rangle_\tau. \quad (6)$$

Consider measurements of $V(\mathbf{x}_3, t)$ and $V(\mathbf{x}_7, t)$ and their instantaneous cross-spectral density,

$$H(\mathbf{d}, \nu, \tau) = W^*(\mathbf{x}_3, \nu, \tau)W(\mathbf{x}_7, \nu, \tau) = |W| \exp(i\phi_{(3,7)}). \quad (7)$$

The instantaneous phase $\phi(\mathbf{d}, \nu, \tau) = \arctan[\Im(H(\mathbf{d}, \nu, \tau))/\Re(H(\mathbf{d}, \nu, \tau))]$ must account for the full separation vector of these pins, that is

$$\phi_{(3,7)}(\mathbf{d}, \nu, \tau) = \mathbf{k}(\nu) \cdot \mathbf{d} = k_r d^r + k_\Theta d^\Theta + k_\zeta d^\zeta, \quad (8)$$

where subscripts (r, Θ, ζ) correspond to radial, poloidal and toroidal directions, respectively.

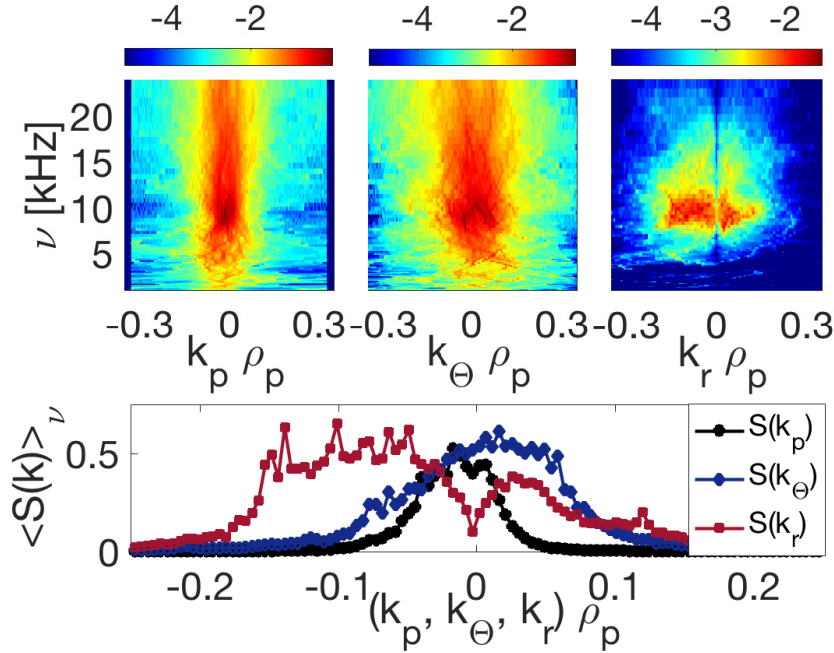


Figure 5. Top row: Comparison of the wave number-frequency spectra for: (left) total wave number projected onto the separation vector as given by (3), (centre) averaged poloidal wave number from pin pairs (1,3) and (7,9) and (right) radial wave number calculated from (10) and (11). Lower panel: power integrated over seven consecutive frequency cuts through each wave number-frequency spectra shown in the top row. Black circles: $S(k_p)$, blue diamond: $S(k_\Theta)$ and red squares: $S(k_r)$.

In what follows we assume the toroidal symmetry of the low frequency modes and neglect the term $k_\zeta d_\zeta$ in (8). We account for the poloidal wave number contribution to $\phi_{(3,7)}$ by considering pin pairs with poloidal and toroidal (neglected) separations only, here pairs (1,3), and (7,9). Neglecting toroidal mode numbers we have $\phi_{(3,7)} =$

$k_r d^r + k_\Theta d_{(3,7)}^\Theta$, $\phi_{(1,3)} = k_\Theta d_{(1,3)}^\Theta$ and $\phi_{(7,9)} = k_\Theta d_{(7,9)}^\Theta$. Adding last two expressions we obtain poloidal wave number

$$k_\Theta = \frac{\phi_{(1,3)} + \phi_{(7,9)}}{d_{(1,3)}^\Theta + d_{(7,9)}^\Theta}. \quad (9)$$

Substituting this to (8) we obtain the corrected estimation of the radial wave number k_r , for a given value of k_Θ :

$$k_r = \left(\phi_{(3,7)} - \frac{[\phi_{(7,9)} + \phi_{(1,3)}]d_{(3,7)}^\Theta}{d_{(7,9)}^\Theta + d_{(1,3)}^\Theta} \right) \frac{1}{d^r}. \quad (10)$$

While the relations $k_r(\nu)$ and $k_\Theta(\nu)$ can be uniquely calculated from equation (10) and (9), the wavenumber-frequency spectrum $S_{(3,7)}[k(k_r, k_\Theta), \nu]$ is still a function of the total wave number k . We will demonstrate later that $S_{3,7}(k, \nu)$, taken as an estimate of the radial wave number-frequency spectrum, underestimates radial wave number range significantly. The quantity $S_{(3,7)}(k, \nu)$ is essentially a probability distribution function of finding a given amount of power at a (k, ν) pair [21]. Using the invariance of probability, we can express $S_{(3,7)}[k(k_r, k_\Theta), \nu]$ as a function of k_r

$$S_{(3,7)}[k(k_r, k_\Theta), \nu] dk d\nu = \frac{k_r}{k} S_{(3,7)}[k_r(k, k_\Theta), \nu] dk_r d\nu, \quad (11)$$

where we have used $k^2 = k_r^2 + k_\Theta^2$. The wavenumber-frequency spectrum is then calculated as

$$S_{(3,7)}(k_r | k_\Theta, \nu) = \langle (|W(\mathbf{r}_3, \nu)|^2 + |W(\mathbf{r}_7, \nu)|^2) \delta(k - k_r) \delta(k - k_\Theta) \rangle \quad (12)$$

and it is treated as a conditional probability of finding a given power at a wave number k_r , for a given value of k_Θ . The equivalent quantity computed from pairs (1, 3) and (7, 9) is simply given by

$$S(k_\Theta, \nu) = \langle (|W(\mathbf{r}_{1(7)}, \nu)|^2 + |W(\mathbf{r}_{3(9)}, \nu)|^2) \delta(k - k_\Theta) \rangle. \quad (13)$$

Using the usual definition of a reduced probability distribution, we then obtain an approximate spectrum of radial wave numbers at a given frequency,

$$S(k_r, \nu) = \sum_{k_\Theta} S_{(3,7)}(k_r | k_\Theta, \nu) S(k_\Theta, \nu). \quad (14)$$

We assume that the Doppler shift at these low frequencies is small and can be neglected. Finally, the direction of propagation will be commented on when results are presented, and it can be verified by the visual inspection of the signals on both pins. In our case, negative k_r values correspond to outward propagation, from the core toward the edge of the tokamak.

4. Results and Discussion

Before we discuss results obtained for different intervals, we use interval A to demonstrate the difference between a wave number-frequency spectra constructed by different methods. The top row of Figure 5 shows three wave number-frequency spectra:

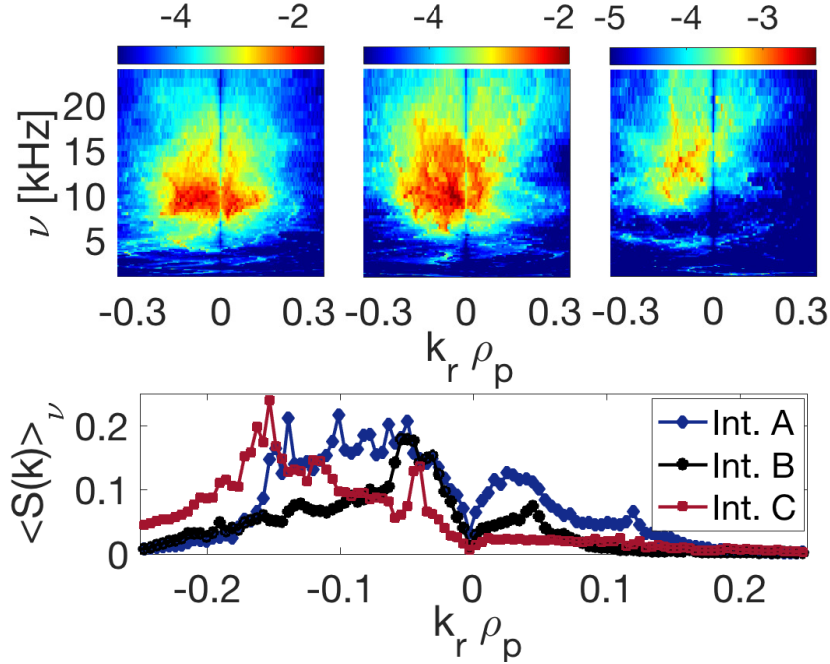


Figure 6. Top row: the wave number-frequency spectra $S(k_r, \nu)$ for: (left) interval A, (centre) interval B and (left) interval C. Lower panel: power integrated over seven consecutive frequency cuts through each wave number-frequency spectra shown in the top row. Blue diamond: interval A, black circles: interval B and red squares: interval C.

on the left is the spectrum $S(k_p, \nu)$ calculated by expression (3), that is, finding the projection of the total wave number on the separation vector, at the centre we plot average poloidal wave number spectrum from pin pairs (1, 3) and (7, 9) and on the right we show $S(k_r, \nu)$ calculated from (10) and (11). The lower panel shows power integrated over seven consecutive frequency cuts, for $9.2\text{kHz} < \nu < 11.0\text{kHz}$ through each wave number-frequency spectra shown in the top row. It is clear that the averaged $S(k_p)$ (black circles) peaks near zero, while the averaged $S(k_r)$ curve (red squares) spans $k_r \rho_p \approx 0.05 - 0.15$. We note that the colour scale corresponds to $\log_{10}(S)$, and the colour scale has been forced to display power near its maximum level, for clarity. These histograms of power have been constructed by dividing the frequency domain into 189 dyadic bins, and dividing the allowed wave number domain of $(-\pi/d, \pi/d)$ into 256 uniform bins. This gives the wave number resolution of $\Delta k \approx 0.03\text{cm}^{-1}$, which corresponds to a minimum wave number of $m = \pm 1$ mode at the geodesic of the edge of MAST plasma.

Figure 6 presents the main result of our study in the format similar to that of figure 5. The top row shows reduced wave number-frequency spectra $S(k_r, \nu)$ for all three intervals, ordered from A on the left to C on the right. The spectrum for interval A is narrow in frequency range and spans a wide range of radial wave numbers $k_r \rho_p \approx 0.05 - 0.15$. The spectrum broadens significantly when the probe moves deeper

into the plasma. Intriguingly, the wavelet spectrum in figure 4 and the $S(k_r, \nu)$ for interval B show high power at ~ 10 kHz and ~ 15 kHz, suggesting that a 10 kHz signal represents a second harmonic of a low power ~ 5 kHz mode. We note that the linear theory predicts zero amplitude of the fundamental GAM harmonic at the mid-plane, but a non-linearly generated second harmonic would have maximum amplitude at this location [23]. Finally, the spectrum for interval C is very narrow, with the clear localisation of the mode at $k_r \approx 0.15$. There are clearly visible linear features in the $S(k_r, \nu)$ plot for interval C . These are more likely local dispersion relation as the probe moves a considerable distance in this interval. We note a lack of any significant power in counter-propagating waves for interval C (no signal at positive k_r), while such peaks at $k_r \rho_p \approx +0.05$ are present in intervals A and B .

It is rather difficult to construct an error estimate for the $S(k_r, \nu)$ spectrum. As a statistically averaged quantity, $S(k_r, \nu)$ can show high values from singular large amplitude fluctuations, which can be rare and thus not statistically significant. In order to make sure that the estimated power comes from the statistically significant number of fluctuations we construct a count histogram, which quantifies a number of samples contributing to each (k_r, ν) pair of interval A . This histogram is shown in the Figure 7. The colour map corresponds to the logarithm of counts. It is clear that there are large number of samples detected in the region of maximal power in $S(k_r, \nu)$. We conclude

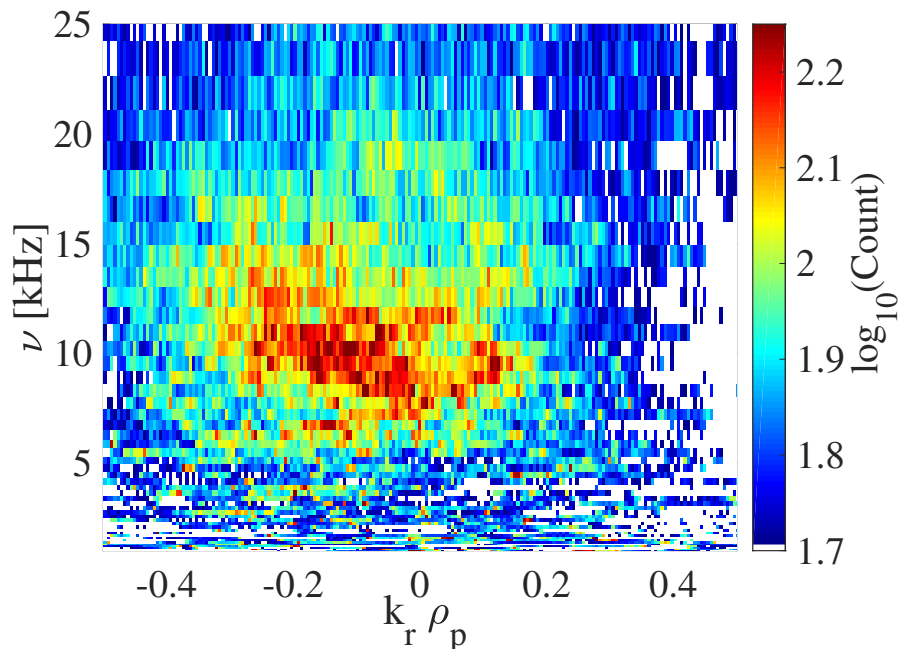


Figure 7. Number of samples contributing to $S(k_r, \nu)$ of interval A .

that the maximal radial wave number of GAM-like fluctuations at frequency $\nu \approx 10$ kHz is $k_r = -1.15$ [1/cm]. This corresponds to wavelength of $\lambda \approx 6$ cm. The estimated phase velocity is in the range of $v^{ph} \approx 1$ km/s. These values are lower than, but broadly

consistent with results obtained from the multi-fluid simulations for MAST [17] L-mode discharges with realistic elongation. The measured wave number is also consistent with the qualitative estimates based on drift/ITG turbulence simulations, which find the most unstable mode number at $k_{\Theta}\rho_p \approx 0.3$. The nonlinear interactions transfer the energy towards large scale, until other mechanisms terminate the transfer. Assuming that at the termination scale we reached approximate isotropy so that $k_{\Theta} \approx k_r$, our estimate of $\leq k_r\rho_p \approx 0.15$ appears to be reasonable.

Measured k_r values allow estimation of the shearing rate of the oscillatory flows, which is approximately given as $\gamma_{sh} \approx k_r v_{\Theta,GAM}$. We calculate $v_{\Theta,GAM} \approx (\Delta E_r)/B_0$, where ΔE_r is taken as a standard deviation of the radial electric field $E_r(t) \approx 0.5 * [V(\mathbf{x}_3, t) - V(\mathbf{x}_7, t)]/d^r$ (the radial and poloidal separation for pins 3 and 7 are nearly the same). This gives an estimate $v_{\Theta,GAM} \approx 2 \times 10^3$ m/s, leading to $\gamma_{sh} \approx 1 \times 10^4$ [1/s]. This value is much smaller than a typical growth rate of the drift instability, $\gamma_{dr} \approx 10^5$ [1/s].

5. Conclusions

In summary, we have obtained a first estimate of the radial wave number k_r of the GAM-like oscillatory flows in the Ohmic MAST edge plasma discharge. The GAM signal appears when the probe depth is about 2 cm into the plasma and the frequency is close to 10kHz, in agreement with previous observations and numerical simulations [15, 17]. We find maximum radial mode number of $k_r\rho_p \approx -0.15$. This estimate gives the radial phase velocity of the GAM of 1 km s⁻¹ and a shearing rate that is about one order of magnitude smaller than the typical growth rate of drift instability in MAST edge plasma.

Acknowledgments

This work was part-funded by the RCUK Energy Programme under grant EP/I501045 and the European Communities under the contract of Association between EURATOM and CCFE. The views and opinions expressed herein do not necessarily reflect those of the European Commission.

- [1] Diamond P H, Itoh S I, Itoh K and Hahm T S 2005 *Plasma Phys. Control. Fusion* **47** R35
- [2] Lin Z, Hahm T S, Lee W W, Tang W M and White R B 1998 *Science* **281** 1835
- [3] Terry P W, Newman D E and Ware A S 2001 *Phys. Rev. Lett.* **87** 185001
- [4] B. N. Rogers, W. Dorland, and M. Kotschenreuther, *Phys. Rev. Lett.* **85**, 5336 2000
- [5] Moyer R A, Tynan G R, Holland C and Burin M J 2001 *Phys. Rev. Lett.* **87** 135001
- [6] Tynan G R et al. 2001 *Phys. Plasmas* **8** 2691
- [7] Hasegawa A and Wakatani M 1987 *Phys. Rev. Lett.* **59** 1581
- [8] Winsor N, Johnson J L and Dawson J M 1968 *Phys. Fluids* **11** 2448
- [9] Lakhin V P, Ilgisonis V I and Smolyakov A I 2010 *Phys Lett. A*, **374** 4872
- [10] Gao Z 2011 *Phys. Plasmas* **17** 092503
- [11] V I Ilgisonis, I V Khalzov, V P Lakhin, A I Smolyakov, E A Sorokina *Plasma Phys. Control. Fusion* **56** 2014
- [12] Jakubowski M, Fonck R J and McKee G R 2002 *Phys. Rev. Lett.* **89** 265003

Experimental constraint on the radial mode number of the Geodesic Acoustic Mode in MAST Ohmic plasma.

- [13] Ido T et.al., 2006 *Plasma Phys. Control. Fusion* 48 S41
- [14] Conway G D 2008 *Plasma Phys. Control. Fusion* **50** 124026
- [15] Robinson J R, Hnat B et al submitted *Plasma Phys. Control. Fusion* 2012
- [16] N. Miyoto, Y. Kishimoto, and J. Q. Li, *Plasma Phys. Controlled Fusion* 48, A335 2006.
- [17] J. R. Robinson, B. Hnat, A. Thyagaraja, K. G. McClements, P. J. Knight, A. Kirk and the MAST Team, *Phys. Plasmas* 20, 052302 (2013).
- [18] Scott B, 2003, *Phys. Lett. A* 32053
- [19] K. Miki and P. H. Diamond, *Phys. Plasmas* 17, 032309 (2010); doi: <http://dx.doi.org/10.1063/1.3353037>
- [20] K. Itoh K, S.-I. Itoh, P. H. Diamond, A. Fujisawa, M. Yagi, T. Watari, Y. Nagashima, and A. Fukuyama, *J. Plasma Fusion Res.* 1, 037 2006.
- [21] Beall, J. M., Kim, Y. C., and Powers, E. J. 1982, *J. Appl. Phys.*, 53, 3933, doi: 10.1063/1.331279
- [22] MacLatchy C S et.al., 1992 *Rev. Sci. Instrum.* 633923
- [23] Fu, G. Y. "On nonlinear self-interaction of geodesic acoustic mode driven by energetic particles." *Journal of Plasma Physics* 77.4 (2011): 457-467.